Supplemental Material: Low-excitation transport and separation of high-mass-ratio mixed-species ion chains

F. Lancellotti,[1,*] S. Welte,[1,†] M. Simoni,[1] C. Mordini,[1] T. Behrle,[1] B. de Neeve,[1] M. Marinelli,[1,‡] V. Negnevitsky,[1,§] and J. P. Home[1,2,¶]

[1] *Institute for Quantum Electronics, ETH Zürich, Otto-Stern-Weg 1, 8093 Zürich, Switzerland*
[2] *Quantum Center, ETH Zürich, 8093 Zürich, Switzerland*

SEGMENTED THREE-DIMENSIONAL ION TRAP.

The ion trap is composed of a multi-layer three-dimensional chip made from gold-plated alumina wafers [S1, S2]. The two RF electrodes are operated at ∼380 V with a frequency of 113.5 MHz. The DC electrodes are controlled by a voltage range of [-10, +10] V and their sizes vary from 155 µm to 1000 µm depending on the trap region. The DC electrodes are filtered with low-pass filters with a cut-off frequency of 68 kHz. The ion-electrode distance is 184 µm.

FITTING OF BLUE SIDEBAND FLOPS FOR PHONON POPULATION EXTRACTION.

To extract the phonon population of a mode of interest we drive a blue sideband pulse of varying duration for a fixed initial internal state and subsequently read out the spin. We then fit the experimental data with a model of the form [S1]

$$P(\downarrow,t)=\frac{1}{2}\sum_{n=0}^{n_{\max}}p(n)\Big(1+\exp(-\gamma_n t)\cos(\Omega_{n,n+1}t)\Big) \quad (1)$$

where $p(n)$ is the probability to find the oscillator in the n$^{\text{th}}$ energy eigenstate, $\Omega_{n,n+1}$ is the Rabi frequency for the transition between the states $|\downarrow\rangle|n\rangle$ and $|\uparrow\rangle|n+1\rangle$ and γ_n is a phenomenological decay rate which accounts for decoherence and intensity fluctuations in the applied laser pulses. When the distribution of the probabilities $p(n)$ is thermal we use

$$p(n)=\frac{\bar{n}_{\text{th}}^{n}}{(\bar{n}_{\text{th}}+1)^{n+1}}, \quad (2)$$

while when $p(n)$ is a displaced thermal state distribution we use [S3]

$$p(n)=\sum_{m=0}^{n_{max}}\frac{\bar{n}_{\text{th}}^{m}}{(\bar{n}_{\text{th}}+1)^{m+1}}e^{-|\alpha|^2}|\alpha|^{2(n+m)}m!n! \times\left|\sum_{l=0}^{m}(-1)^l\frac{|\alpha|^{-2l}}{l!(m-l)!(n-l)!}\right|^2. \quad (3)$$

We employ the definition

$$\Omega_{n,n+1}=\Omega e^{-\eta^2/2}\sqrt{\frac{1}{n+1}}\eta L_n^1(\eta^2), \quad (4)$$

where η is the Lamb-Dicke parameter, which in our experiment is $\eta_{Be}\simeq 0.4$ and $\eta_{Ca}\simeq 0.06$ for the ^{9}Be$^+$ and ^{40}Ca$^+$ ions in each individual well respectively. For the Be–Ca crystal, the Lamb-Dicke parameters are $\eta_{Be}\simeq 0.3$ for the mode Z2 and $\eta_{Ca}\simeq 0.05$ for the mode Z1. $L_n^1(\eta^2)$ denotes the generalized Laguerre polynomial [S1]. For fitting the data, we use the thermal mean phonon number $\bar{n}_{\text{th}}$, the coherent mean phonon number $|\alpha|^2$, the decay rate γ_n and the Rabi frequency Ω as free fit parameters, and truncate the sum in Eq.1 to $n_{\max}=20$, significantly more than the observed average phonon numbers.

Fig.S1 shows an example of data taken in the transport and separation experiments. The Be–Ca crystal is transported and subsequently separated as described in the main text. Then, a blue sideband flop is performed to extract the mean phonon number in the axial direction of the ^{40}Ca$^+$ ion. Subsequently, the ions are transported in parallel to transfer the ^{9}Be$^+$ ion into the detection zone before a readout pulse allows us to extract the excitation in the axial trap direction. The data is fitted with the model from equations 1 and 2.

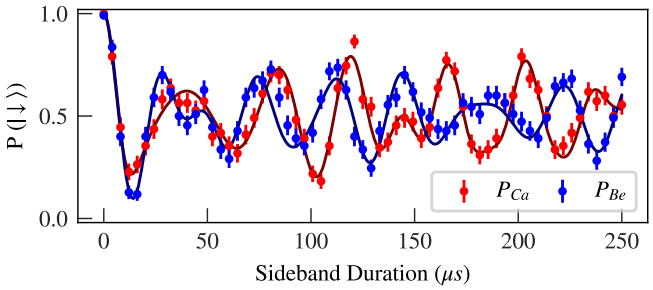

FIG. S1: Extrapolation of phonon population in the axial motional mode of ^{40}Ca$^+$ (red) and ^{9}Be$^+$ (blue) after the transport and separation sequence T2–S2–PT. From the fit of eq. 1 (solid lines), we extract mean phonon numbers of $\bar{n}=1.40(8)$ for the calcium ion and $\bar{n}=1.44(9)$ for the beryllium ion.

MICROMOTION COMPENSATION

Radial micromotion is detected through the excitation of radial modes by resonant parametric modulation of the RF voltage. When the ion is far from the RF null, the motion is excited, which reduces the ion fluorescence

in a subsequent detection [S4]. We compensate stray fields by applying voltages to electrodes on additional wafers of the trap stack [S5]. To perform the compensation at any arbitrary point in the waveform sequence, the latter is run up to that position and subsequently the RF parametric modulation is switched on while setting specific compensating voltages. The sequence is then reversed and the ion fluorescence is detected. We choose the compensating voltages that prevent ion excitation. This procedure can be applied to any point in the trap, even for those without laser beam access. Before running the transport waveform, the micromotion is compensated at 11 discrete points in the waveform which are evenly distributed over the entire transport time. During the separation waveform, the micromotion is compensated at 12 discrete points. In between these discrete points, we linearly interpolate the micromotion compensation voltages. This calibration is performed automatically and needs to be repeated about once per month.

VOLTAGE WAVEFORMS

The waveforms we employ for the transport and separation of the ion chains are generated through a numerical quadratic programming algorithm [S5]. Once smooth ion trajectories and mode frequency profiles are defined, the solver finds the optimal voltages that minimize a cost function and satisfy specific constraints, e.g. DAC voltage limits, voltage slew rate, direction of vibrational modes relevant for cooling, etc. Additionally, the waveforms are tested and optimized experimentally. An example of ion trajectory and mode frequencies related to the transport and separation waveforms T2-S2 is shown in Fig.S2. The Python library we developed for the generation and analysis of the waveforms has been released as an open-source package [S6].

SINGLE SPECIES SEPARATION

In Fig.4(a) of the main text we analyze the performance of the mixed-species ion chain separation while executing it at different speeds. Here we show results of similar measurements of the excitations induced by separating single-species ion crystals composed of Ca–Ca and Be–Be. The results are shown in Fig.S3. In this measurement, the transport waveform works at 26% lower axial frequency for a single $^{40}Ca^{+}$ than for the waveforms used in the main text. During this protocol, the radial mode Y1 crosses twice with the axial mode Z2 for Ca–Ca crystal without any quadrupole being applied, so the amount of coupling between the modes has not been quantified nor controlled. This crossing does not happen for Be–Be chains.

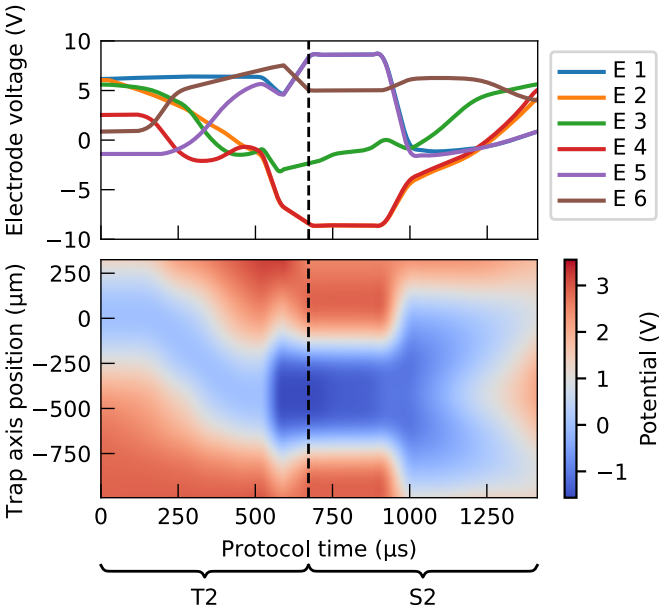

FIG. S2: Voltages applied to the relevant trap electrodes shown in Fig.1 of the main text (top) and generated potentials at the trap axis (bottom) while running the transport (T2) and separation (S2) waveforms. The origin of the trap position axis corresponds to the center of electrode 5, shown in the trap schematic in Fig.1 of the main text.

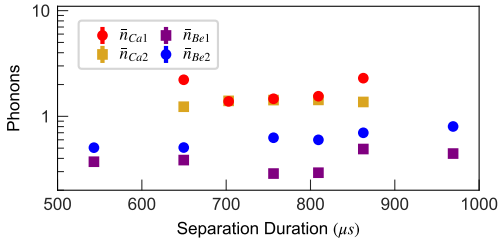

FIG. S3: Separation of Ca-Ca and Be-Be crystals. The index 1 indicates the ion trapped in the first well that reaches the detection zone after separation, while the index 2 indicates the ion that arrives after parallel transport.

COMPARISON OF SEPARATION EXCITATION FOR BE–CA AND CA–BE

In the main text, we report that separating Ca–Be crystals induces higher excitations in the Z1 mode than with Be–Ca. In particular, we find excitations after the separation sequence T2-S2-PT of $\bar{n}_{Ca}$=3.8(6) and $\bar{n}_{Be}$=0.24(3).

We observe a few differences between the two configurations. First, we find that the optimal value of the applied axial field depends on the crystal order, which we attribute to the presence of a pseudopotential gradient along the trap axis [S7]. Measurements of the trap

frequencies of the mixed-species chains close to the critical point are shown in the upper panel of Fig.S4. We observe that the minimum value of the Z1 frequency and the time in the waveform at which this is achieved is different in the two cases. We suspect that these differences are due to asymmetric anharmonic terms in the potential, or to the differences in position of the ions in the potential in the two different cases. Measurements of the heating rates of two configurations at different points in the waveform are shown in the lower panel of Fig.S4. These show a considerable difference between the two orders, which occurs at a point where the mode with the higher heating rate has a higher frequency. We do not know why this occurs, but it may relate to uncontrolled orientation of the ion chain close to the critical point. We note that radial modes (such as Y2) aligned between our DC electrodes exhibit high heating rates in the presence of a radial field and it is possible that the Ca–Be axial modes align with this at some point.

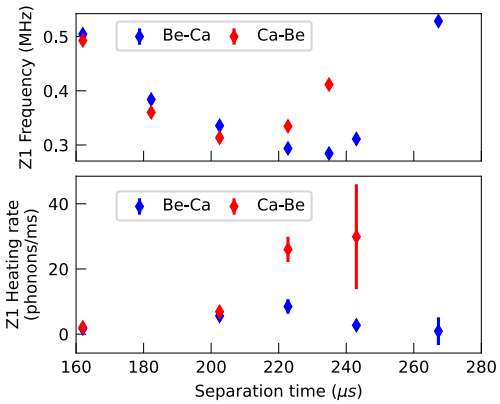

FIG. S4: Z1 frequency and heating rate measurements for the Be–Ca and Ca–Be configurations as a function of time during the separation protocol.

SEPARATING LARGER ION CRYSTALS

We also tested the separation of larger ion crystals using the same separation waveform used for the two-ion crystal employed so far. To this end, we separated an ion crystal constituted by three ions (Ca–Be–Ca and Be–Ca–Be) and four ions (Ca–Be–Ca–Be). In these measurements, we did not measure the excitation of the ions after the separation process but we did verify that the crystal can be separated arbitrarily into two parts with low loss of fluorescence. As shown in Fig.S5, depending on an axial field applied to the ions in the separation zone, different numbers of ions can be separated to the left or right well. The results show that in this process the ion order is reliably maintained. We observe a loss of fluorescence counts only for the cases where three or more ions are in well 2.

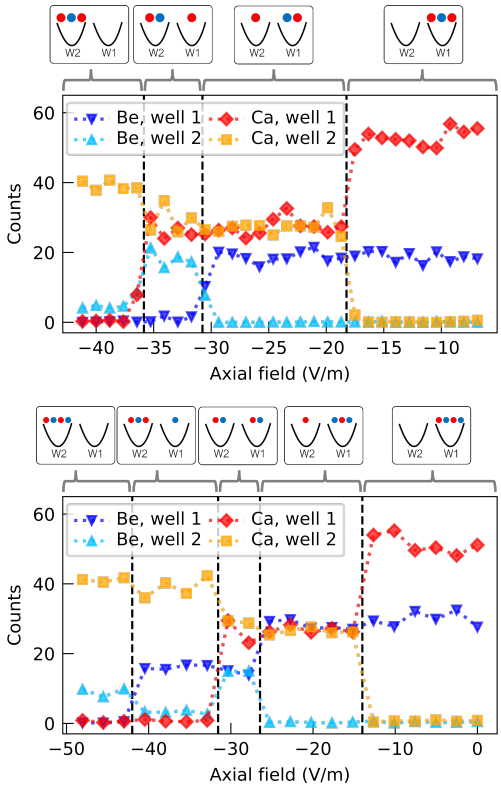

FIG. S5: Fluorescence counts detected in the two final wells after separating Ca–Be–Ca (top) and Ca–Be–Ca–Be (bottom) ion crystals as a function of the axial field. On top of the plots, the small graphs show the final ion configurations.

* E-mail: flancell@phys.ethz.ch
† E-mail: weltes@phys.ethz.ch
‡ Current address: JILA, Boulder, Colorado, USA
§ Current address: Oxford Ionics, Oxford, OX5 1PF, United Kingdom
¶ E-mail: jhome@phys.ethz.ch

[S1] Daniel Kienzler. *Quantum harmonic oscillator state synthesis by reservoir engineering.* PhD Thesis, ETH Zurich (2015).

[S2] L. E. de Clercq, H.-Y. Lo, M. Marinelli, D. Nadlinger, R. Oswald, V. Negnevitsky, D. Kienzler, B. Keitch, and J.P. Home. *Parallel Transport Quantum Logic Gates with Trapped Ions.* Physical Review Letters **116**, 080502 (2016).

[S3] T. Ruster, C. Warschburger, H. Kaufmann, C.T. Schmiegelow, A. Walter, M. Hettrich, A. Pfister, V. Kaushal, F. Schmidt-Kaler, and U.G. Poschinger. *Experimental realization of fast ion separation in segmented Paul traps.* Physical Review A **90**, 033410 (2014).

[S4] Y. Ibaraki, U. Tanaka, and S. Urabe. *Detection of parametric resonance of trapped ions for micromotion compensation.* Applied Physics B **105**, 219–223 (2011).

[S5] V. Negnevitsky. *Feedback-stabilised quantum states in a mixed-species ion system.* PhD Thesis, ETH Zurich (2018).

[S6] C. Mordini, F. Lancellotti, V. Negnevitsky, M. Marinelli, R. Oswald, and T. Saegesser. *Pytrans.* Zenodo, v2.1.0+a (2023).

[S7] J. P. Home. *Quantum Science and Metrology with Mixed-Species Ion Chains.* Advances In Atomic, Molecular, and Optical Physics (edited by E. Arimondo, P. R. Berman, and C. C. Li) **62**, 231–277 (2013).